A semi-automatic interpretation method for utilizing InSAR results to recognize active landslides considering causative factors

Weiming Liao[1,2], Pengyuan Liu[2], Yanfei Kang[2]*, Lichuan Chen[2], Manqian Liu[2] and Minyan Liao[2]

[1]Key Laboratory of High-speed Railway Engineering, Ministry of Education, Southwest Jiaotong University, Chengdu, China, [2]Technology Innovation Center of Geohazards Automatic Monitoring, Ministry of Natural Resources, Chongqing Institute of Geology and Mineral Resources, Chongqing, China

Synthetic Aperture Radar Interferometry (InSAR), which can map subtle ground displacement over large areas, has been widely utilized to recognize active landslides. Nevertheless, due to various origins of subtle ground displacement, their presence on slopes may not always reflect the occurrence of active landslides. Therefore, interpretation of exact landslide-correlated deformation from InSAR results can be very challenging, especially in mountainous areas, where natural phenomenon like soil creep, anthropogenic activities and erroneous deformational signals accumulated during InSAR processing can easily lead to misinterpretation. In this paper, a two-phase interpretation method applicable to regional-scale active landslide recognition utilizing InSAR results is presented. The first phase utilizes statistical threshold and clustering analysis to detect unstable regions mapped by InSAR. The second phase introduces landslide susceptibility combined with empirical rainfall threshold, which are considered as causative factors for active landslides triggered by rainfall, to screen unstable regions indicative of active landslides. A case study validated by field survey indicates that the proposed interpretation method, when compared to a baseline model reported in the literature, can achieve better interpretation accuracy and miss rate.

1 Introduction

Landslides are a sign of slope instability, which can transform into disastrous events due to natural or anthropogenic triggering factors (Varnes, 1984). To mitigate such risks, recognition of active landslides before catastrophic collapse is a primary goal of current research (Lacroix et al., 2020). Active landslides can be generally described with a three-state creep behavior, including a secondary creep that accumulates subtle

displacements constantly (Intrieri et al., 2019). Therefore, ground displacements have often been utilized as an important sign for recognizing active landslides (Pu et al., 2023). However, such ground displacements are not registered routinely, especially in mountainous regions, because of the high cost involved in field survey and *in-situ* instrumentation. In recent years, interferometric synthetic aperture radar (InSAR), capable of capturing millimetric ground displacement from space, has become a consolidated tool for the landslide community (Bekaert et al., 2020). Indeed, satellite-based InSAR has been widely used to recognize active landslides without prior knowledge of their location since the early 2000s (Ferretti et al., 2001). With the improvement of SAR satellites that provide an unprecedented time series dataset of InSAR (Ho Tong Minh et al., 2020), mapping active landslides utilizing InSAR results, from national (Di Martire et al., 2017; Festa et al., 2022), regional (Zhang et al., 2018), and basin (Zhang et al., 2016; Jia et al., 2022) levels, has been adopted by both developed and developing countries.

Nevertheless, focusing on practical aspects of recognizing active landslides in mountainous regions, processing SAR datasets and interpreting InSAR results can be very challenging. For instance, landslide-prone regions are typically distributed in alpine canyon areas with vegetation coverage, where signal decorrelations, geometric distortion, and phase wrapping inevitably limit the reliable extraction of ground surface deformation from the entire interferograms (Ho Tong Minh et al., 2020). Besides, the current satellite acquisition frequency and the one-dimensional nature of the InSAR results impose physical constraints on capturing the three-dimensional and nonlinear kinematics of landslides. Furthermore, as emphasized by Wasowski and Bovenga (2014), subtle ground displacements measured by InSAR can have different origins, without distinguishing the origins of their motion, this may lead to misleading results. Milillo et al. (2022) reported practical research combining InSAR results with machine learning methods to recognize active landslides automatically. However, they also reported misinterpreted results localized in non-landslide areas, which were attributed to anthropogenic activities such as oil field extraction or aquifer use. Necula et al. (2021) reported a more complicated case of misinterpretation in which ground displacement mapped by InSAR was attributed to the construction of residential buildings over in-active landslides. In summary, inevitable signal noise during InSAR processing in landslide-prone regions and the difficulty in discriminating landslide-correlated deformation in InSAR results are ongoing challenges. Although InSAR processing is crucial to obtain reasonable ground deformation measurements, the present study only focuses on the interpretation of InSAR results (e.g., interferograms, IFs; mean velocity maps, MVMs). Therefore, from the perspective of radar interpretation defined by Farina et al. (2006), InSAR results require careful interpretation before they can be reliably considered as active landslides.

To reduce erroneous interpretations of InSAR results for the purpose of landslide recognition (also reported as landslide detection or identification in the literature), various interpreting methods have been proposed over the last decade. In addition to visual interpretation by experts (Ponziani et al., 2023), combining velocity threshold with clustering analysis (e.g., unsupervised machine learning algorithms, UMLAs) has been widely utilized

to interpret active landslides from InSAR results: fixed threshold reported by Righini et al. (2012), statistical threshold reported by Aslan et al. (2020), hot-spot analysis reported by Lu et al. (2019), C-index reported by Xiong et al. (2023), index of separating trend reported by Li et al. (2023). Furthermore, by applying landslide predisposing factors (e.g., slope angle, lithology, land use, and others), which have been used in landslide susceptibility analysis, researchers have attempted to explicitly link InSAR-mapped ground displacements to active landslide.

With the expansion of large SAR archives and processing techniques (Ho Tong Minh et al., 2020), interpreting large volumes of InSAR datasets automatically has become crucial nowadays, especially for large scale engineering applications. From the aspect of practical interests, interpretation of InSAR data to recognize active landslides can be further divided into two processes, which include unstable regions detection (also called anomalies detection reported by (Raspini et al., 2018) and root-cause analysis of ground deformation phenomena, respectively. Festa et al. (2022) reported a pioneering work in semi-automatic interpretation of nation-wide InSAR results to recognize various natural hazards. The unstable regions detection process was accomplished by applying spatial clustering to obtain moving area clusters. The root-cause analysis process was done by introducing ancillary data like landslide inventory maps, vertical-horizontal component ratios obtained through 2D-decomposition of LOS displacements, and minimum slope angle threshold. He et al. (2023) reported an interpretation method by combining fixed displacement rate thresholds and landslide susceptibility. By introducing the latter into the root-cause analysis process, they found the interpretation method could further separate InSAR-mapped deformation correlated to active landslides from others. However, the aforementioned threshold, factors or input parameters used during interpretation may not be confidently determined, and they should be case-specific to account for the complex characteristics of different slopes, as well as measurement precision for the given InSAR results (Cigna et al., 2013).

In addition, supervised machine learning algorithms (SMLAs) have been introduced for interpreting InSAR results to recognize active landslides recently. Some of these studies only utilized InSAR results as the model input variable, where IFs or MVMs were directly inputted into pre-trained models using different SMLAs. For instance, combining stacked IFs with YOLOv3 reported by Fu et al. (2022), combining MVMs with Faster RCNN reported by Cai et al. (2023). In addition, some other studies, assisted by SMLAs and multi-dimensional datasets containing InSAR results and auxiliary data, were also reported (Novellino et al., 2021). Indeed, many published and unpublished SMLAs studies are addressing in improving accuracy and efficiency of landslide recognition using InSAR results. However, there are still several limitations highlighted in the literature, including dilemmas in constructing an appropriate dataset with limited landslide samples within a given region, and most importantly, introducing landslide triggering mechanisms to improve model interpretability (Novellino et al., 2021).

On the other hand, from the perspective of slope-scale landslide analysis, ground displacement induced by certain causative factors can be evaluated by means of analytical or numerical methods. However, the application of these methods may not be completely justified for regional-scale landslide recognition purposes, especially if all required input data are not available

without prior knowledge of landslides' location. To the best of the authors' knowledge, there have been rather few attempts to connect InSAR results to landslide triggering mechanism for the purpose of recognizing active landslides, especially considering causative factors such as precipitation. For instance, Dong et al. (2023) reported an interpretation method to screen pre-clustered InSAR results. The Pearson correlation coefficient between InSAR-mapped ground displacement time-series and accumulated monthly rainfall combined with landslide susceptibility was introduced into the root-cause analysis. Even though the reported interpretation method only requires a limited number of easily accessible datasets, the simplified statistical relationship between ground displacement and rainfall described by the Pearson correlation coefficient may not represent the sophisticated triggering mechanisms of rain-induced landslides compared with analytical/numerical or other statistical methods.

In this paper, for the purpose of recognizing active landslides at a regional scale, a simple-to-use method for interpreting InSAR results is presented. Taking landslide triggering by seasonal precipitation as an example, we propose a two-phase process to screen InSAR-measured MVMs combining clustering analysis, landslide susceptibility and possibility of rainfall-induced landslide failures. Here we assume that a higher likelihood of landslide failure, as indicated by rainfall thresholds, would correlate with a greater potential for landslide-correlated deformation captured by InSAR. This, in turn, may serve as an indicator for interpreting InSAR results to recognize active landslides. To achieve this, we construct empirical rainfall thresholds to indicate the possibility of landslide failures using satellite-based hourly precipitation data and recorded landslide failure events. After validating this by field surveys, the performance of the proposed method is evaluated and compared with a baseline model reported in the literature. Overall, by explicitly introducing the causative factors into the root-cause analysis, this study provides a semi-automatic interpretation method for discriminating InSAR-mapped deformation results correlated to the unique physical phenomena of rainfall-induced landslides.

2 Study area

The selected study area is Fengjie County, located in the Northeastern Chongqing Municipality, China. Due to its mountainous terrain, complex geological conditions, and unique weather patterns characterized by continuous rainy days and heavy rainfall every autumn (referred to as the West China Autumn Rain), Fengjie County is particularly vulnerable to rainfall-induced landslides (Li et al., 2022). Furthermore, Fengjie County has jurisdiction over 29 towns with approximately 745,000 inhabitants. Due to rapid development, human engineering activities such as land reclamation and housing construction have become significant contributing factors to events related to ground surface deformation (Zhang et al., 2023).

Open-source SAR data have been acquired by Sentinel-1 from the European Space Agency (ESA) to ensure weekly global coverage of the land surface. Due to the impact of Sentinel-1B failure, the acquisition of Sentinel-1A has been affected worldwide, especially in China. As a result, the acquisition percentage (actual acquisition versus planned acquisition) of the Sentinel-1A has degraded in the

study area since 2021. It is worth noting that Sentinel-1A data have acquisitions only in ascending orbits in the study area (See Figure 1). In addition, the digital elevation model (DEM) obtained from the Shuttle Radar Topography Mission (SRTM) and the normalized difference vegetation index (NDVI) derived from Sentinel-2 optical images imply that the area would suffer from geometrical distortion and signal decorrelation.
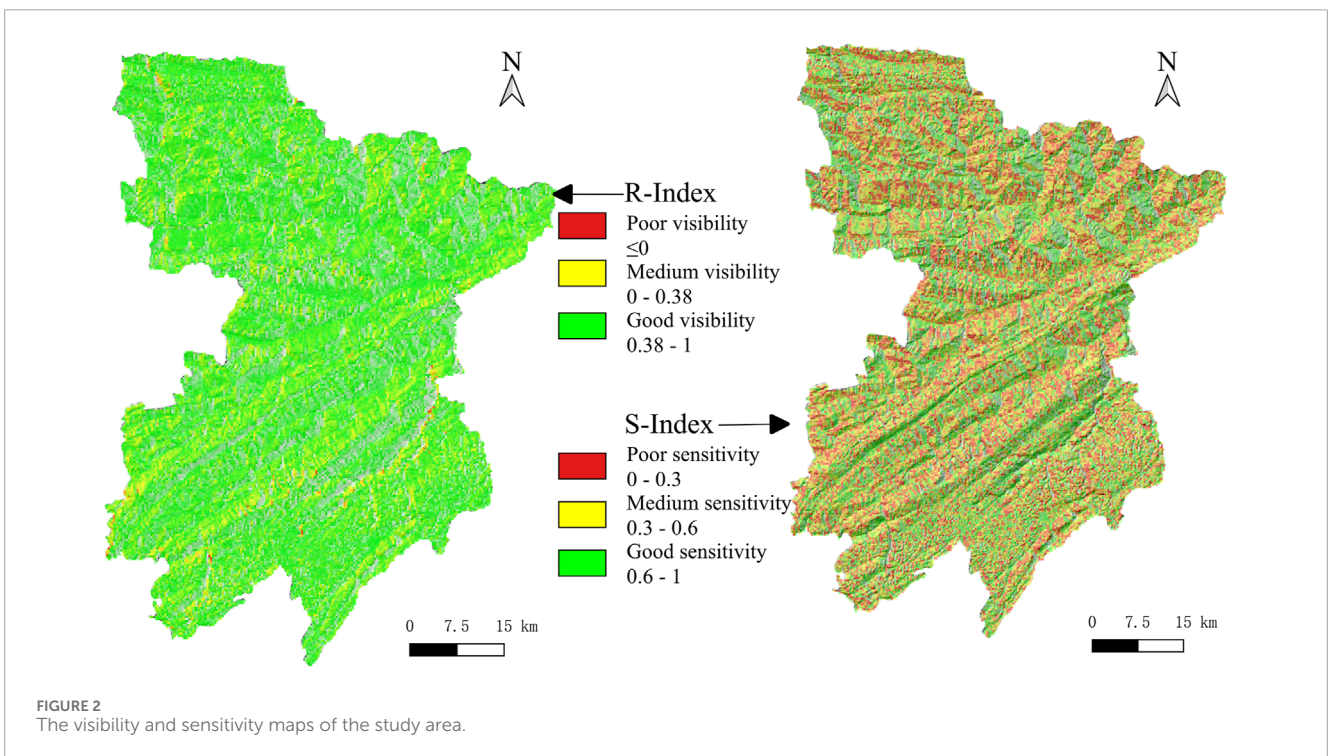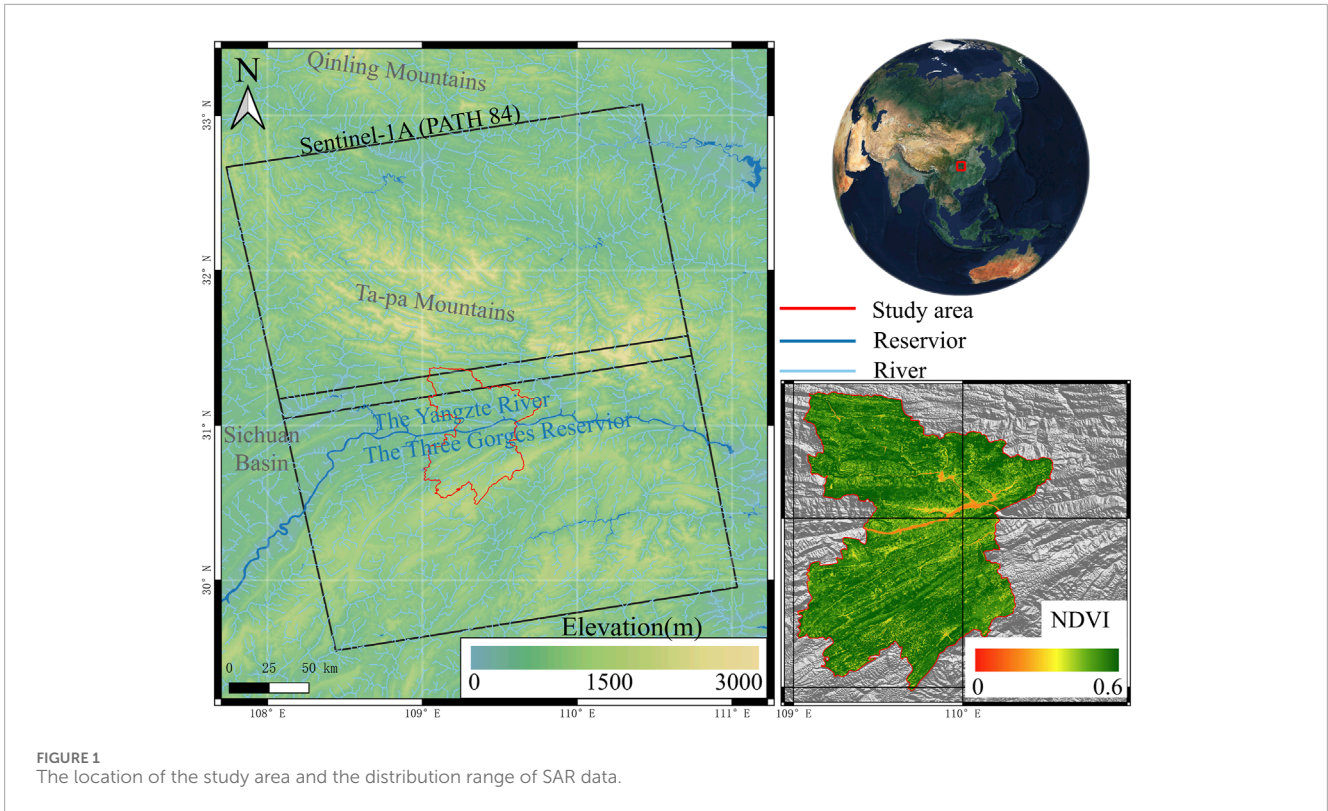
3 Materials and methods

3.1 Data preparation

The application of InSAR results to landslide deformation tracking should satisfy the geometric sensitivity to deformation (van Natijne et al., 2022). Therefore, the applicability of SAR images acquired by Sentinel-1A was analyzed initially. We followed the methods suggested by (Notti et al., 2014; Dai et al., 2022) to create visibility and sensitivity maps of the study area (See Figure 2). The R-index (RI), or range index, has been widely used to assess the topographic effects, specifically the visibility of the SAR image. As indicated by Notti et al. (2014), the RI represents the ratio between the slant range (a radar geometry distance) and the ground range (an Earth surface distance). The RI was classified into three levels, which includes poor, medium, and good visibility, ranging from below 0, 0 to 0.38, and 0.38 to 1, respectively. The S-index (SI), or sensitivity index, was calculated by the orthogonal projection of the downslope unit vector onto the line-of-sight of the radar satellite (Chang et al., 2018). The SI was classified into three levels (Dai et al., 2022), which include poor, medium, and good visibility, ranging from below 0 to 0.3, 0.3 to 0.6 and 0.6 to 1, respectively.

The landslide susceptibility map of the study area was produced by the analytic hierarchy process (AHP), which belongs to the expert's knowledge-based methodology. Twelve conditioning factors were used in the analysis process following the suggestion reported by Gong et al. (2022). Areas with landslide susceptibility values (LSV) among lower than 0.3, 0.3–0.55, 0.55–0.7 and greater than 0.7 were categorized into low, moderate, high, and very high susceptibility, respectively. As illustrated in Figure 3, 79.97% of the study area is referred to as having good RI. However, due to the west-east distribution of the Yangtze River and extrusion from the Ta-Pa Mountains, slopes in the study area may tend to form a north-south orientation along river networks or mountains. As a result, SI in the study area exhibits only 25.68% of good sensitivity. From the perspective of landslide susceptibility, as shown in Figure 3 and reported by other researchers (Zhang et al., 2023), most of the study area exhibits low and moderate susceptibility. Areas with high and very high susceptibility are mainly located along the Yangtze River or low mountain and hilly areas in the northwest part.

To construct empirical rainfall thresholds for the study area, historical data of recorded landslide failures from 2013 to 2019 were collected. Then, data preprocessing was conducted to eliminate improbable data. After that, as illustrated in Figure 3, 951 recorded landslide failure events were utilized in this study. The Precipitation Estimation from Remotely Sensed Information using Artificial Neural Network Cloud Classification System (PERSIANN-CSS), a widely used satellite precipitation product (Nguyen et al., 2019),

FIGURE 1
The location of the study area and the distribution range of SAR data.

FIGURE 2
The visibility and sensitivity maps of the study area.

was utilized as rainfall data. This product has an hourly temporal resolution and a 4 km spatial resolution. PERSIANN-CSS data from 2013 to 2019 were collected, totalling 242 grid cells per hour in the study area. It should be noted that the PERSIANN products tend to overestimate precipitation in high-elevation regions in Southwest China due to fewer rain gauge observations that can be used for correction (Nie and Sun, 2020).

To avoid the influence of irregular Sentinel-1A acquisitions in the study area since 2021, 58 scenes of SAR images were collected from January 1 to 26 December 2020. The processed InSAR data

FIGURE 3
The distribution of recorded landslide failures from 2013 to 2019 and overlayed with landslide susceptibility in the study area. The distribution of R-Index, S-Index, and landslide susceptibility in the study area.
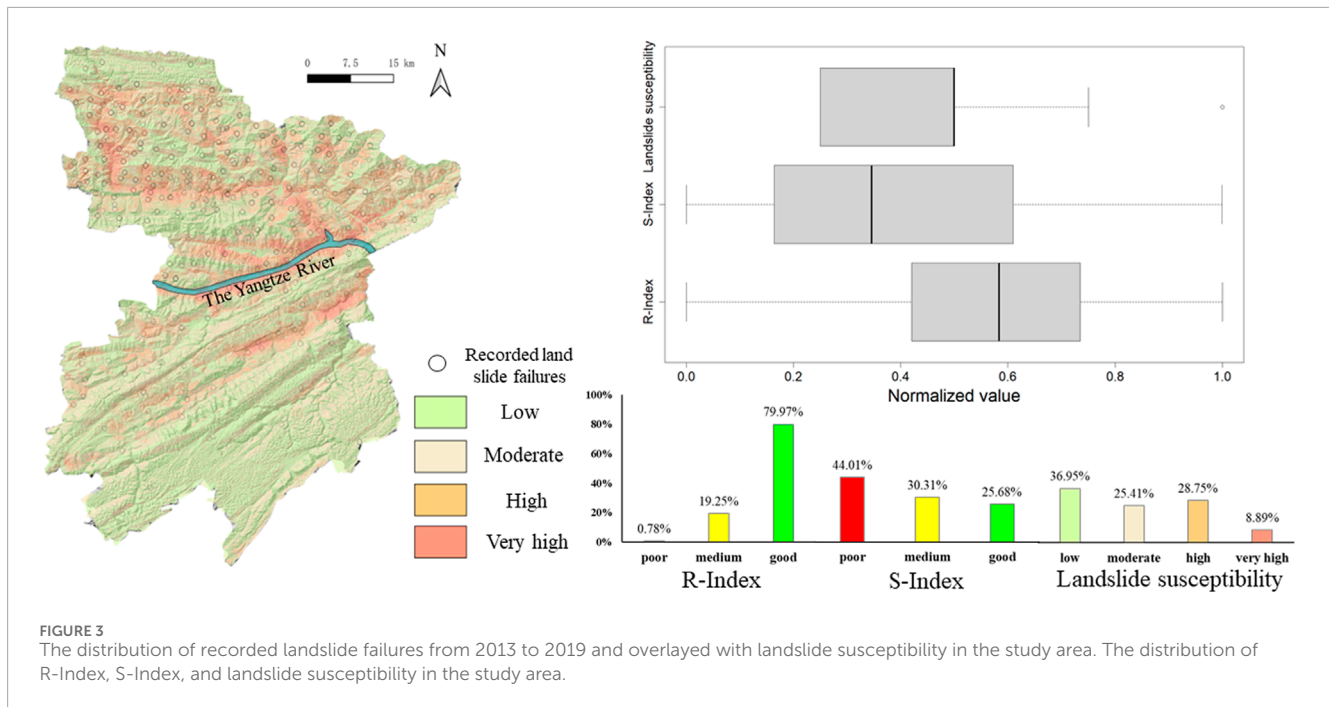
from these SAR images with ascending orbits were used, generating a total of 10,454,266 coherent targets (CTs) in the study area. The final spatial resolution of the InSAR data was 20 × 20 m. Based on the CT density evaluation process suggested by Wang et al. (2021), five land cover types, which include cropland, forest, grassland, water, and bareland, were chosen to evaluate the CT density. As depicted in Figure 4, CT density changes dramatically in different land cover types and can be categorized into three applicability levels. Excluding the land cover type of water, the land cover type of forest, which covers 62% of the total area, has the lowest value of 1398 CT/km^2 and can be classified as having a low applicability level. In contrast, the land cover type of bareland, which covers less than 1% of the total area, has the highest value of 6170 CT/km^2 and can be classified as having a high applicability level. Additionally, CT density in the land cover types of cropland and grassland varies from 4,417 to 4927 CT/km^2 and can be classified as having a medium applicability level.

3.2 Causally-connected method for interpreting InSAR results

As depicted in Figure 5, the proposed interpretation method contains two phases, namely, unstable regions detection (Phase I) and root-cause analysis (Phase II). Clustering analysis combined with statistical thresholds are utilized to detect unstable regions initially. Then, these preliminary results are further evaluated through root-cause analysis considering internal and external attributions that contribute to landslide movements. In particular, landslide susceptibility is introduced as the internal attribution to isolate unstable regions that are located in landslide-prone areas. Additionally, rainfall thresholds, which indicate the possibility of rainfall-induced landslide failures, are introduced as the

external attribution. By screening with landslide susceptibility and reconstructed rainfall thresholds, the unstable regions mapped by InSAR can be isolated to surface movements pointing to active landslides.

3.2.1 Unstable regions detection

Based on previous studies and data conditions in the study area, we first used statistical analysis to obtain CTs with mean annual velocity above 3 times standard deviation (3σ). Then, we used a spatial clustering algorithm called DBSCAN (Pedregosa et al., 2011). According to parameter selection reported by Bakon et al. (2017) and Montalti et al. (2019), three parameters were preset in the DBSCAN algorithm. Eps, which refers to radius for which the CTs are considered reachable, was set as 100 m; MinPts, which refers to a minimum number of neighboring points, was set as 3; Metric was set to haversine to allow data input in the form of latitude and longitude.

3.2.2 Root-cause analysis

Aiming to improve the performance of the interpretation method, the root-cause analysis was further divided into two individual processes in the proposed interpretation method. Landslide susceptibility and rainfall thresholds were introduced to causally connect InSAR-mapped ground deformation to active landslides triggered by rainfall.

After screening CTs through Phase I, clustered polygons were compared with landslide susceptibility, which corresponds to the probability of landslide occurrence across a given geographic space (Loche et al., 2022). Compared with the minimum slope angle threshold reported in the literature, the landslide susceptibility can take slope angle as well as other predisposing factors into consideration. Landslide susceptibility of the study area was obtained by considering twelve conditioning factors, which include elevation, slope angle, aspect, terrain curvature, terrain
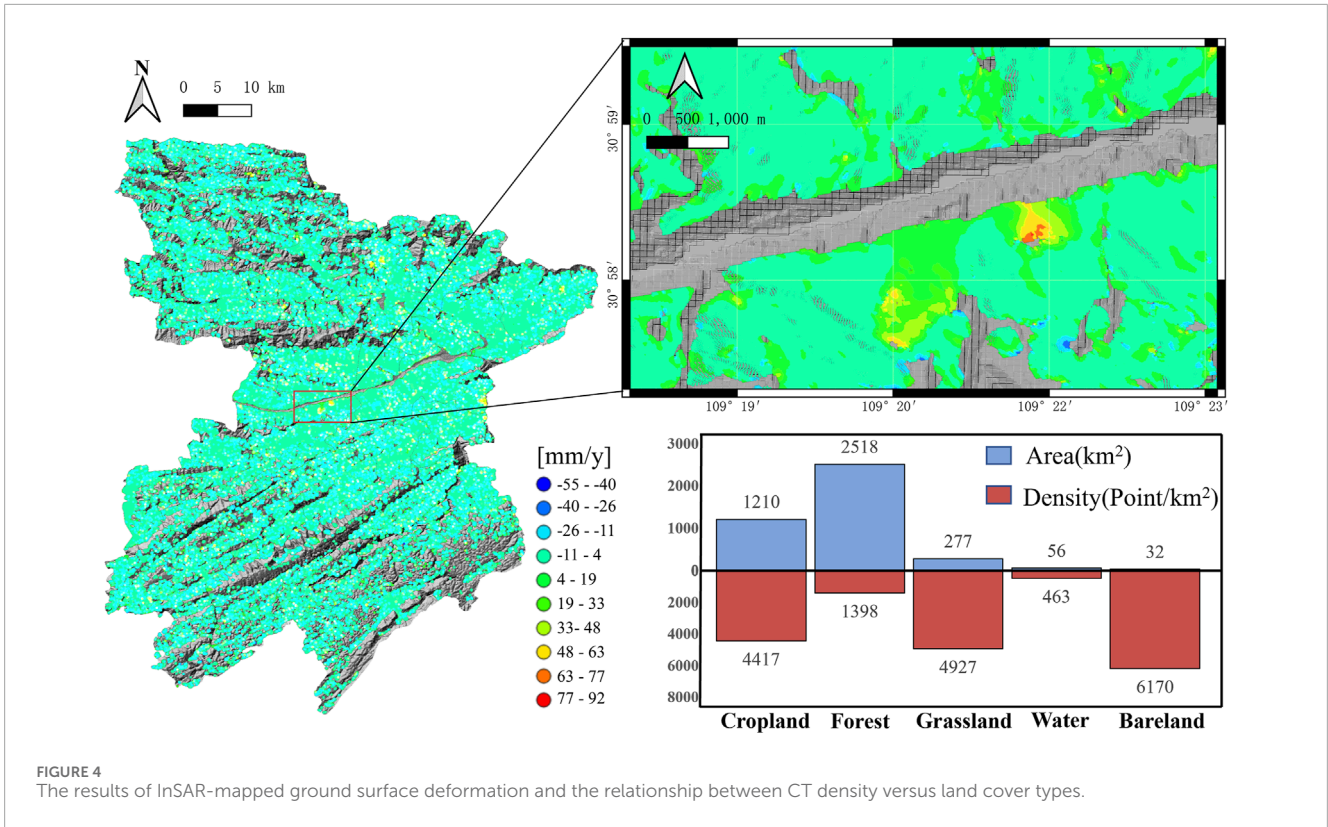
FIGURE 4
The results of InSAR-mapped ground surface deformation and the relationship between CT density versus land cover types.
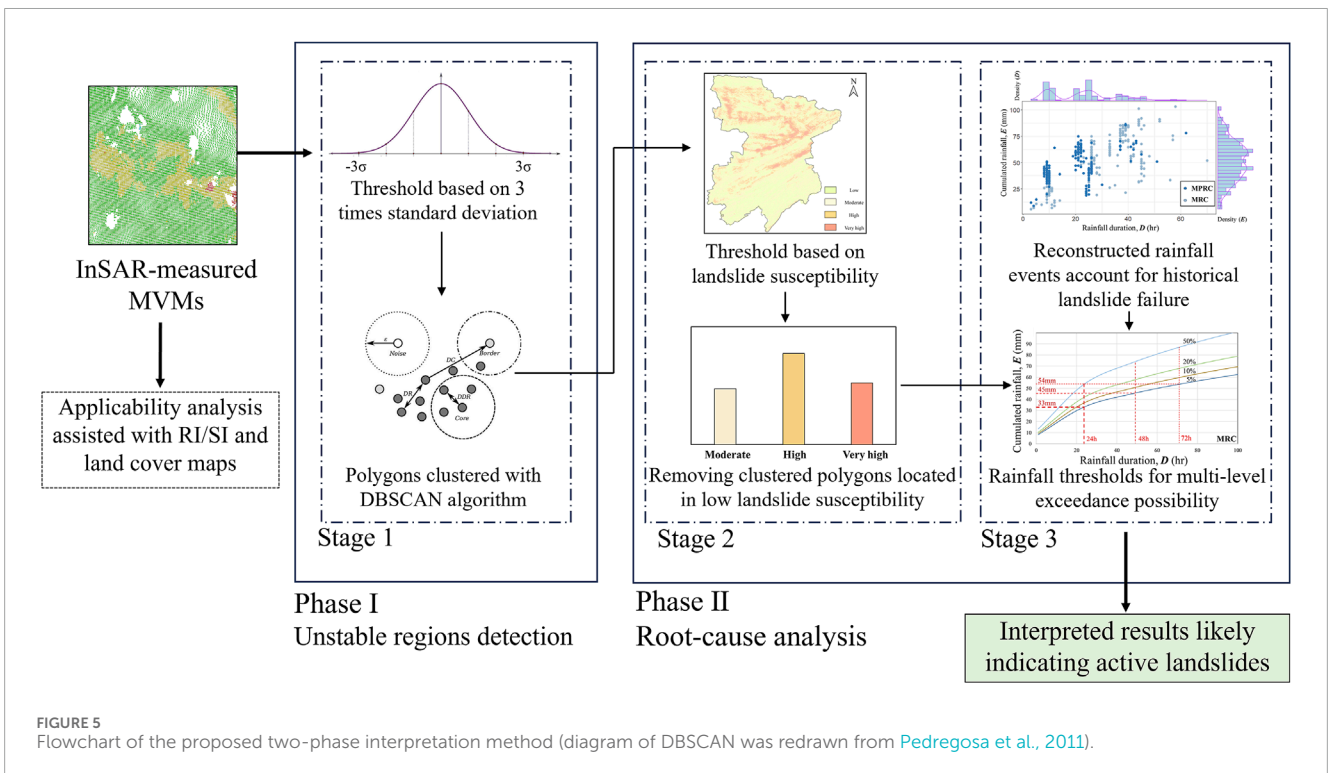

FIGURE 5
Flowchart of the proposed two-phase interpretation method (diagram of DBSCAN was redrawn from Pedregosa et al., 2011).

ruggedness index, lithology, distance to fold, distance to river, stream power index, topographic wetness index, NDVI, and distance to road (Gong et al., 2022). To unify the resolution of conditioning factors, all data were resampled and input at a resolution of

100 m following the suggestion reported by Liu et al. (2023). Clustered polygons with low landslide susceptibility were considered as other ground deformation phenomena captured by InSAR and removed.

The following step was used to introduce the rainfall threshold for indicating the precursory movement before landslide failure. The rainfall threshold is one of the known hydrological conditions (e.g., rainfall, infiltration, soil moisture) that, when reached or exceeded, is likely to trigger landslides (Guzzetti et al., 2007). To obtain such a threshold, the best separators in a Cartesian plane segmenting triggering and non-triggering rainfall conditions need to be extracted from known slope failure events and correlated rainfall records (Crozier, 1997). The most common rainfall thresholds in the literature include rainfall mean intensity versus rainfall duration (I-D) and cumulated event rainfall versus rainfall duration (E-D). In this paper, an E-D type of rainfall threshold was constructed by using a comprehensive tool called CTRL-T (Melillo et al., 2018). The CTRL-T, which includes three main algorithm blocks for rainfall events reconstruction, selection of triggering conditions responsible for the slope failure events, and calculation of rainfall thresholds at different exceedance probabilities (EPs), was written in R open-source software.

The original CTRL-T algorithm requires two types of input data, including rainfall data (rain gauge location, rainfall time series, and event parameters) and landslide data (location and occurrence time). To introduce satellite rainfall products instead of rain gauge observations, we followed the procedures suggested by Rossi et al. (2017). The centroid of each satellite-based rainfall grid cell was treated as a virtual rain gauge, resulting in a total of 242 virtual rain gauges capable of providing hourly precipitation observations in the study area. Like the traditional method of empirical rainfall threshold construction, the CTRL-T involves selecting the rain gauge for each landslide failure to obtain the representative rainfall condition responsible for landslide triggering. Rossi et al. (2017) suggested using buffer analysis with a 5 km radius to identify the rain gauge for mountain regions. Because the distance between each virtual rain gauge (the centroid of each grid cell) is 4 km, less than the buffering radius mentioned above, the closest virtual rain gauge for each landslide failure event was selected in this paper.

After correlating satellite-based rainfall observations to landslide failure events, it is necessary to set reasonable parameters to determine the rainfall event responsible for landslide triggering. Ten parameters were utilized to reconstruct the rainfall events responsible for landslide triggering. A detailed description of these parameters refers to Melillo et al. (2015). As emphasized by Melillo et al. (2015), these parameters, which were primarily suitable for Italy, were empirically determined by experts. It should be noted that the study area belongs to the subtropical monsoon climate with West China Autumn Rain, which is different from the Mediterranean climate in Italy. Therefore, the warm period for the study area was adjusted to April to October according to the characteristics of the subtropical monsoon climate. As illustrated in Table 1, we carefully selected other empirical parameters based on the local meteorological and seasonal conditions.

In the literature, the daily rainfall intensity (DRI) is a widely utilized indicator and shows good predictive power for landslide triggering (Leonarduzzi et al., 2017). Therefore, the maximum daily rainfall intensity (MARI) was utilized as the indicator in the root-cause analysis process. First, based on the E-D type of rainfall threshold derived by the CTRL-T algorithm, lower-bound DRI with different EPs were constructed. Then, the MARI in 2020, which is

TABLE 1 Input parameters for CRTL-T algorithm.

Parameter name	Parameter value		Unit
	Warm periods (C_W)	Cold periods (C_C)	
Gs	0.2	0.2	mm
E_R	0.2	0.2	mm
P_1	6	3	h
P_2	12	6	h
P_3	1	1	mm
P_4	96	48	h
sws	5		month
ews	9		month
R_b	5		km

compatible with InSAR observation, was extracted from gridded satellite precipitation data. Next, clustered polygons distributed in the grids with MARI surpassing certain DRI were considered as interpreted results likely indicating active landslides triggered by rainfall.

3.2.3 Validation of the proposed interpretation method

In order to validate the proposed interpretation method and evaluate its performance, we constructed a baseline model first. Then, results between the proposed and the baseline models were compared and validated through field survey. It should be noted that the Sentinel-1A has only acquired ascending orbits in the study area. As a result, 2D-decomposition of LOS displacements from ascending and descending InSAR observation is not available in the study area. Additionally, the interpretation method reported by Dong et al. (2023) requires InSAR-mapped ground displacement time-series, which would be less feasible for large-scale engineering applications compared to MVMs. Therefore, we utilized the interpretation method reported by He et al. (2023) as the baseline model. We constructed this model by using the same method applied in the proposed model for the process of unstable regions detection. Besides, the root-cause analysis process for the baseline model was conducted by setting a threshold for unstable regions located in areas with high and very high landslide susceptibility.

The union set of interpreted results obtained from the baseline and the proposed models was investigated by evaluating macro deformation, deformation history, and stability in the field, as suggested by Xu et al. (2023). Field survey results were first classified into three levels to quantify whether the ground surface movement can be observed (Liang et al., 2022). The principles of classifications were based on field investigation within the interpreted spatial polygons, which include the deformation phenomenon of local cracks, building and infrastructure, covered vegetation, and existing
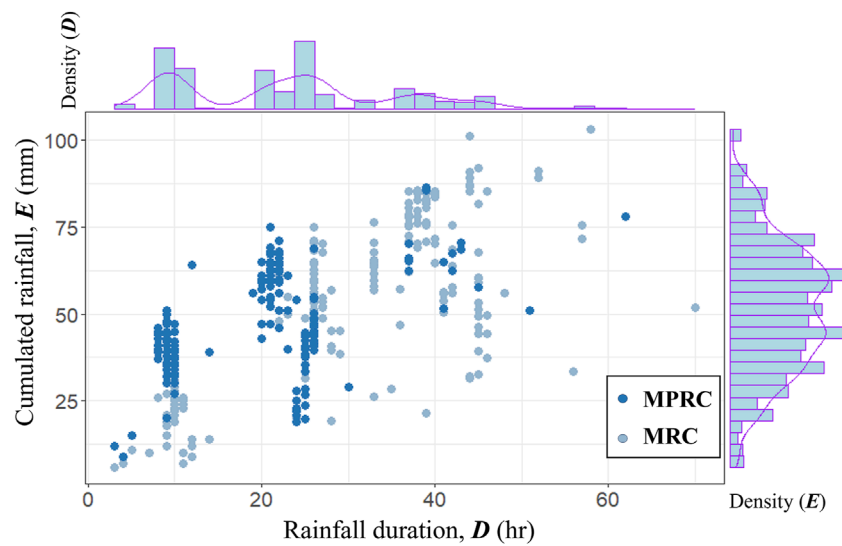
FIGURE 6
The cumulated rainfall and duration of the 813 recorded landslide failure events for MPRCs and MRCs.

landslide mitigation facilities. The deformation phenomenon was divided into distinct deformation (Level I), slight deformation (Level II)), and no obvious deformation (Level III), respectively. After that, field survey results were categorized into three groups, which include landslide-correlated deformation (Category I), ground surface movement induced by other triggering factors (Category II), and no identifiable ground surface movement (Category III). Finally, by comparing the results between the baseline and the proposed model assisted by a confusion matrix, the performance of the proposed interpretation method was evaluated.

4 Results

4.1 Rainfall thresholds for the study area

As shown in Figure 6, 2,251 rainfall events were reconstructed in the study area. Maximum cumulated rainfall in 24 h for these events ranged between 20 and 157 mm. Additionally, by evaluating the delay between the rainfall ending time and the landslide occurrence time for each failure event, a delay longer than 48 h was considered as an indicator for incorrectly dated landslide failure events (Melillo et al., 2018). By applying this criterion, 813 recorded landslide failure events were utilized to construct the rainfall threshold.

After connecting each landslide failure event with the corresponding rainfall event, maximum probability rainfall conditions (MPRCs) and multiple rainfall conditions (MRCs) were reconstructed to obtain rainfall duration (DL) and cumulated event rainfall (EL), respectively. The MPRCs are the subset of MRCs with the highest weight ω, which is proportional to the inverse square distance between the rain gauge and the landslide, the EL, and the rainfall mean intensity. It should be noted that the weight ω is attributed to each DL - EL pair of the MRCs. When the difference in the EL between one pair and the subsequent is less than 10%, the

weight ω attributed to the latter pair is null. Figure 6 illustrates the results of the MPRCs and the MRCs. For the 813 recorded landslide failure events, 1623 DL - EL pairs for MRCs and 834 DL - EL pairs for MPRCs were reconstructed. Table 2 shows the power-law function of empirical rainfall thresholds at 5%, 10%, and 20% Eps, as well as uncertainty associated with the threshold parameters and their respective uncertainties.

After obtaining empirical rainfall thresholds illustrated in Table 2, critical cumulated rainfall for various durations was calculated. As shown in Figure 7, cumulated rainfall for durations of 24 h (daily), 48 h (2-day), and 96 h (3-day) with 5% EP are marked with dashed lines for the two datasets. At a certain EP level, the difference in the cumulated rainfall between the MPRC and the MRC dataset increases with duration. Additionally, similar increasing trends of difference between the two datasets also appear with the increase of the EP. Using the lower-bound value of thresholds derived from the two datasets, DRI can be obtained to indicate the precursory movement for landslide triggering. For 5%, 10%, and 20% EPs, the corresponding DRIs are 29 mm/day, 32 mm/day, and 37 mm/day, respectively.

4.2 Interpreted results based on the baseline and the proposed model

It should be noted that, by applying threshold to unstable regions located in areas with high or very high landslide susceptibility, the baseline model interpreted 52 spatial polygons of unstable regions as active landslides, where 31 and 21 spatial polygons were located in high and very high landslide susceptibility, respectively. In contrast, by combining landslide susceptibility and rainfall threshold, the proposed model utilizing 5% EP interpreted 71 spatial polygons of unstable regions as active landslides. However, applying 10% and 20% EP can only interpret 38 and 23 spatial polygons of unstable regions as active landslides.

TABLE 2 Empirical rainfall thresholds at different EPs.

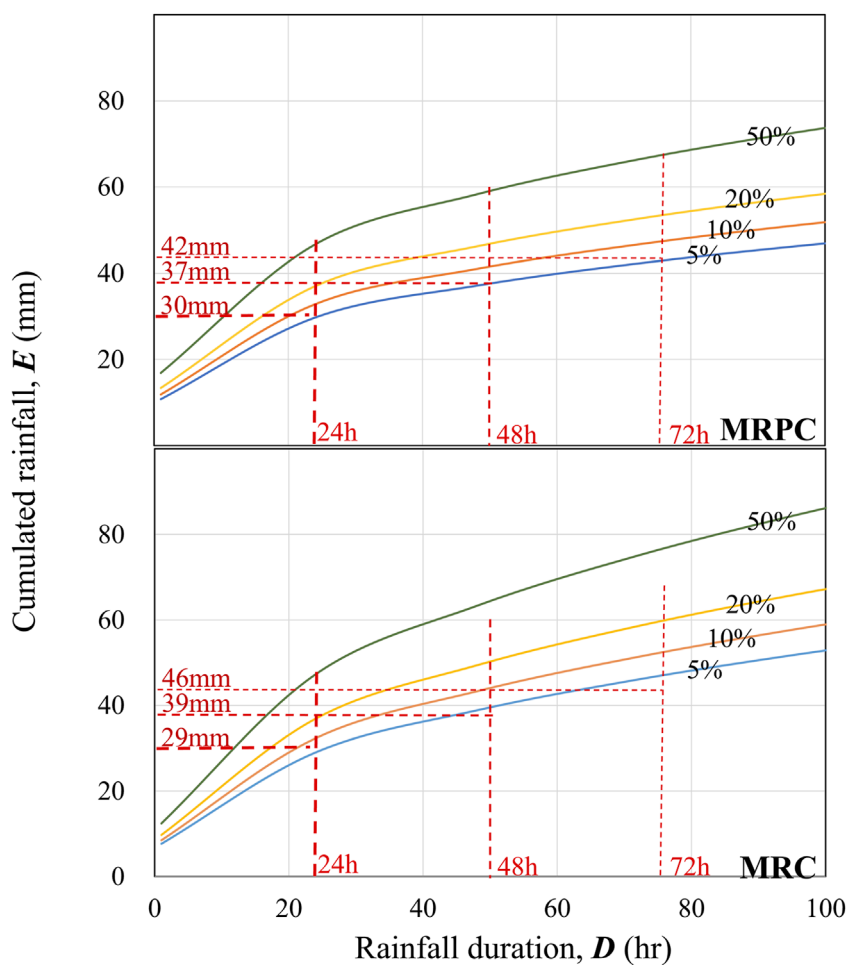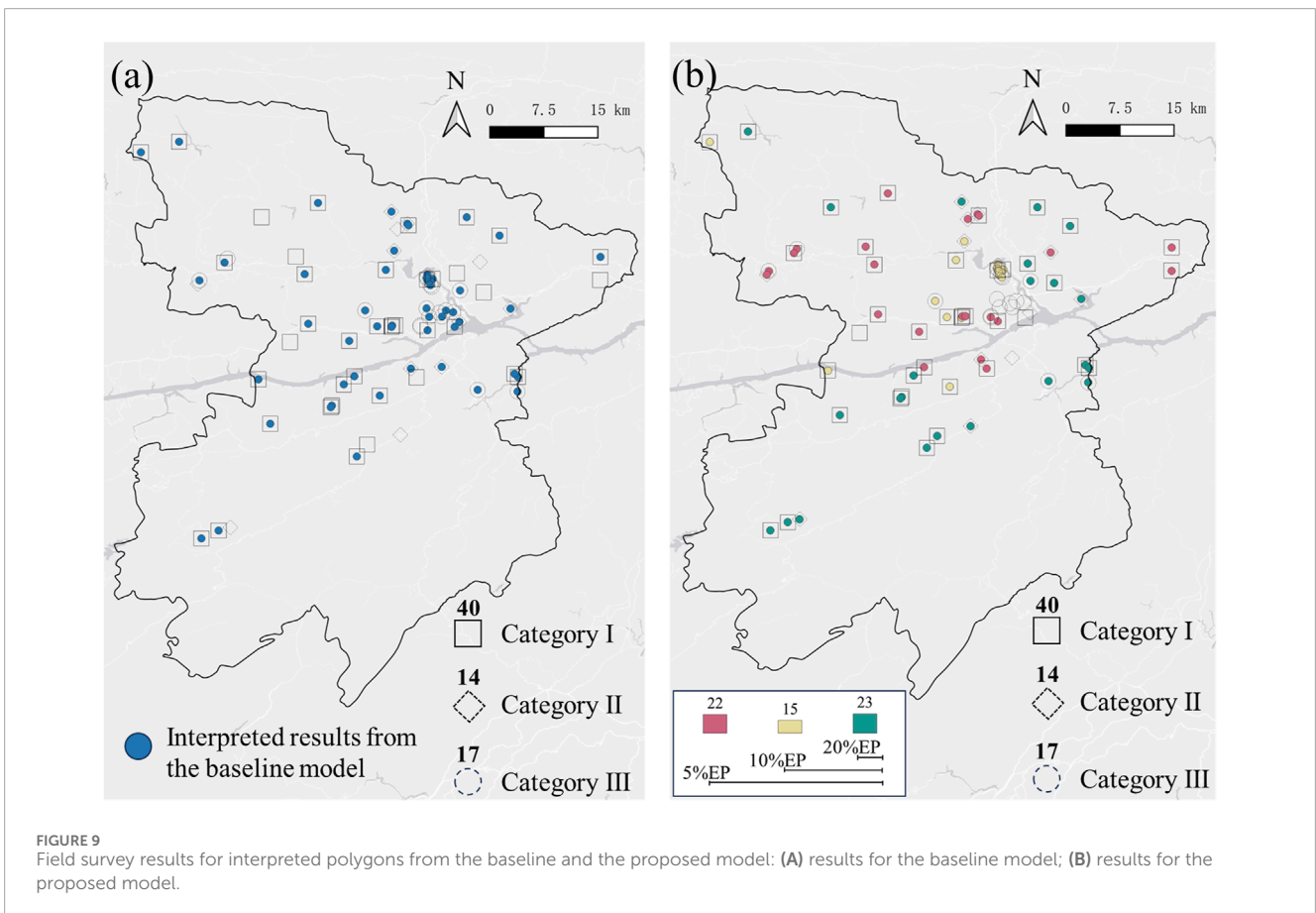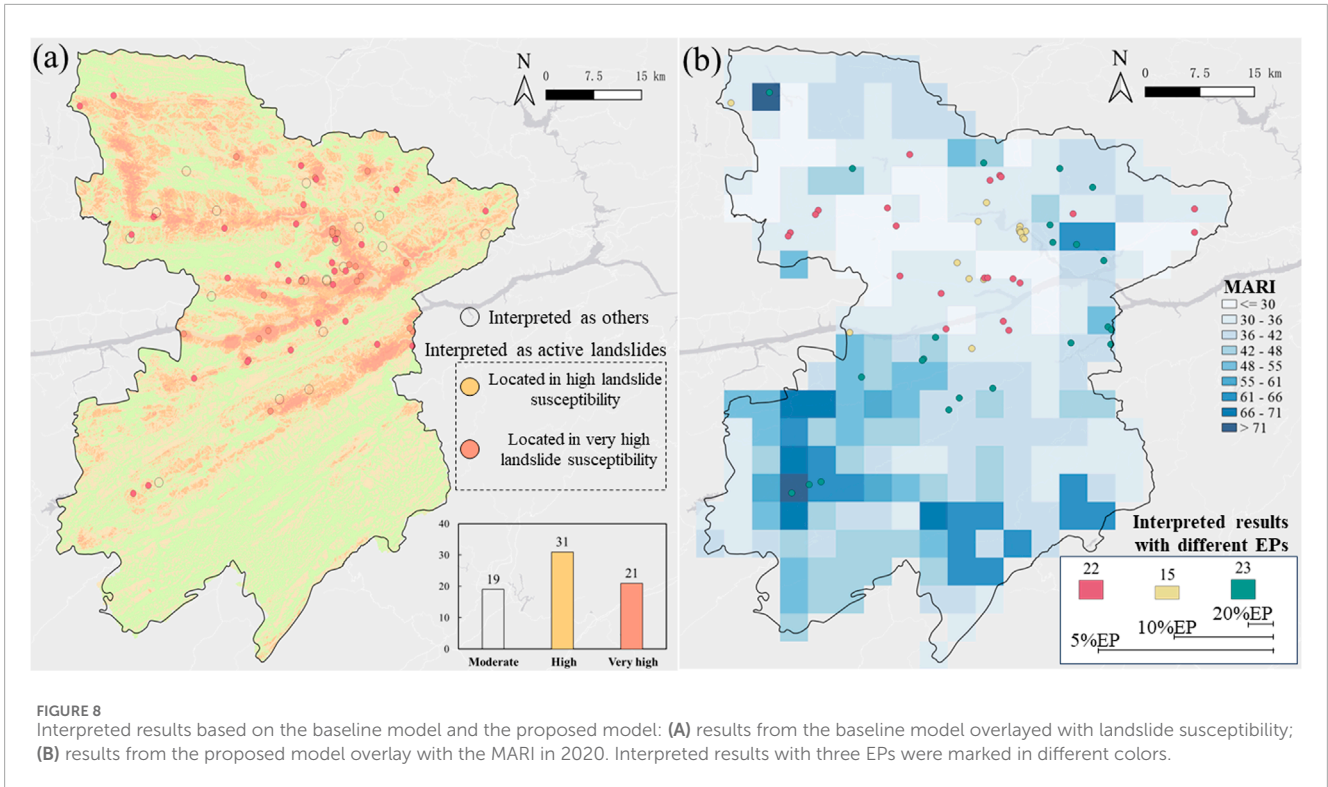| EPs (%)	Power-law function $E = (\alpha \pm \Delta\alpha) \times D^{(\gamma \pm \Delta\gamma)}$	Uncertainty ($\Delta\alpha/\alpha$) (%)	Uncertainty ($\Delta\gamma/\gamma$) (%)	Dataset
5	$E = (11.61 \pm 0.87) \times D^{(0.34 \pm 0.02)}$	7.53	5.88	
10	$E = (12.81 \pm 0.94) \times D^{(0.34 \pm 0.02)}$	7.35	5.88	MPRC
20	$E = (14.42 \pm 1.03) \times D^{(0.34 \pm 0.02)}$	7.13	5.88	
5	$E = (8.23 \pm 0.59) \times D^{(0.44 \pm 0.02)}$	7.16	4.54	
10	$E = (9.16 \pm 0.64) \times D^{(0.44 \pm 0.02)}$	6.98	4.54	MRC
20	$E = (10.42 \pm 0.70) \times D^{(0.44 \pm 0.02)}$	6.78	4.54	

FIGURE 7
The critical cumulated rainfall for durations of 24 h, 48 h, and 72 h under different EPs.

In order to illustrate the difference in interpreted results between the baseline and the proposed model directly, the union set of interpreted results obtained from the two models is illustrated in Figure 8. As shown in Figure 8A, 19 spatial polygons interpreted by the proposed model with 5% EP were interpreted as others by utilizing the baseline model. Figure 8B depicts interpreted results of the proposed model with three rainfall thresholds, which are 5%, 10% and 20% EPs. As shown in Figure 8B, by applying 5%EP during the interpretation process, 71 spatial polygons were all located in grids with DRI surpassing 29 mm/day. That is to say, these polygons of unstable regions were all interpreted as active landslides. In contrast, applying 10% EP would interpret 22 spatial polygons as others, while applying 20% EP would interpret an additional 15 spatial polygons as others.

FIGURE 8
Interpreted results based on the baseline model and the proposed model: **(A)** results from the baseline model overlayed with landslide susceptibility; **(B)** results from the proposed model overlay with the MARI in 2020. Interpreted results with three EPs were marked in different colors.

FIGURE 9
Field survey results for interpreted polygons from the baseline and the proposed model: **(A)** results for the baseline model; **(B)** results for the proposed model.
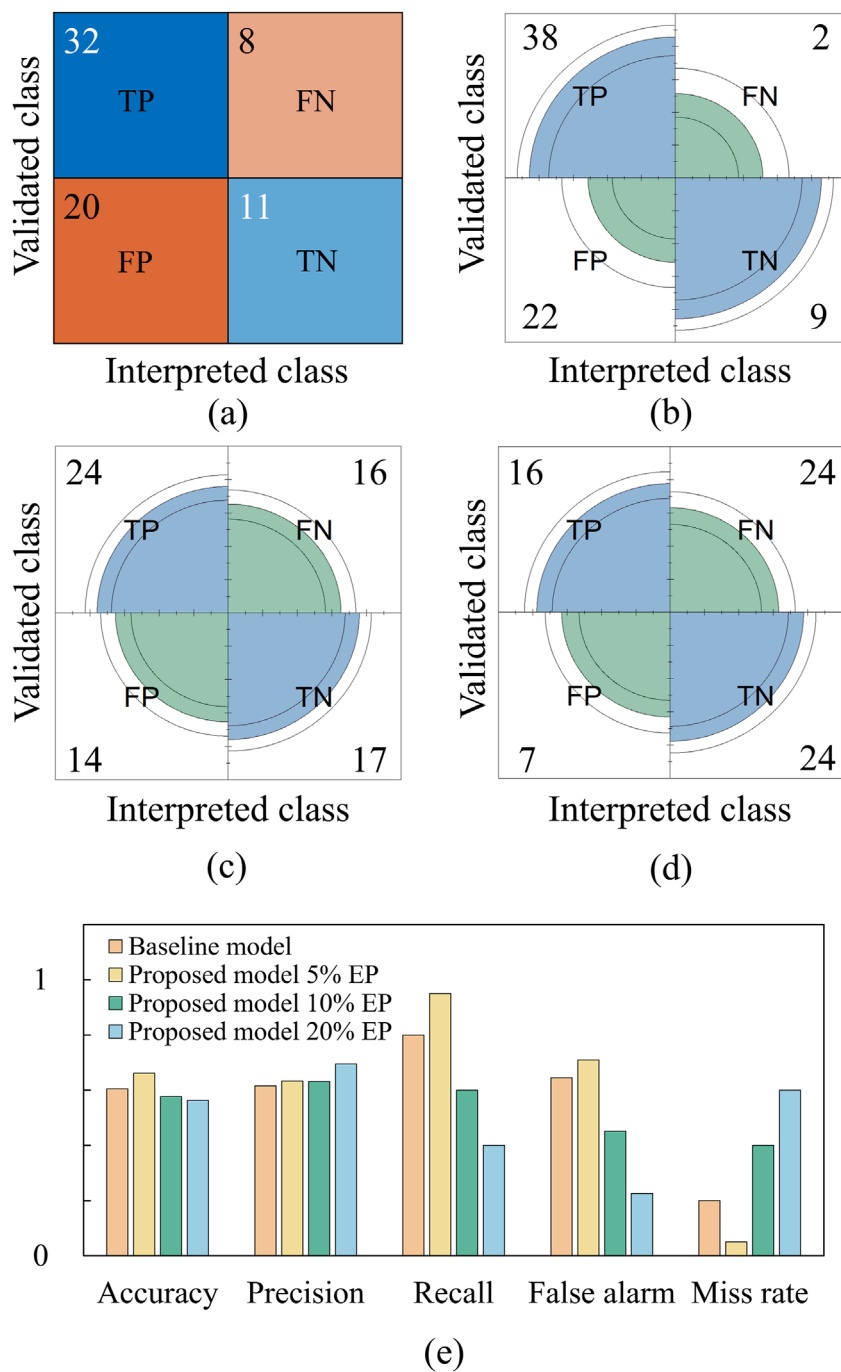
FIGURE 10
Confusion matrices for the baseline and the proposed model, where TP refers to true positive; TN refers to true negative; FN refers to false negative; FP refers to false positive: **(A)** the baseline model; **(B)** the proposed model with 5% EP; **(C)** the proposed model with 10% EP; **(E)** the proposed model with 20% EP; **(E)** accuracy, precision, recall, false alarm and miss rate for different models.

4.3 Validation and evaluation of the proposed interpretation method

By conducting field surveys for 71 spatial polygons, the deformation phenomenon of interpreted results was classified into three levels, as discussed previously. Level I contains 21 interpreted polygons that can be observed as distinct deformation in the field, primarily rupture and cracks on the ground surface or identifiable cracks on the buildings and roads within the polygon area. In contrast, 34 interpreted polygons, 48% of the total polygons, can be subsumed into Level II. These interpreted polygons mainly showed identifiable cracks in the infrastructures. Additionally, Level III includes 17 interpreted polygons. It should be noted that 13 interpreted polygons of Level III were found covering newly-increased farmland. The main culprit for these polygons could be farm work on the slopes. Based on a comprehensive analysis of
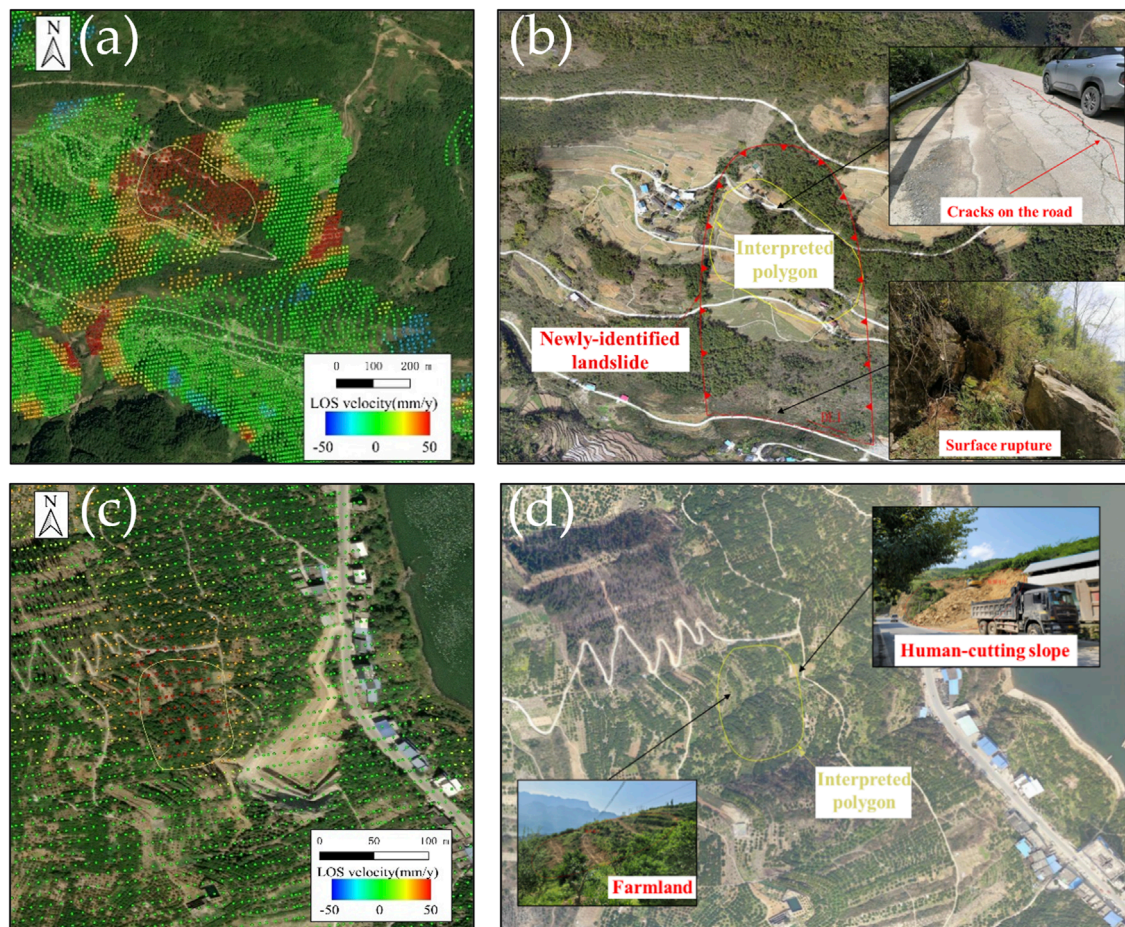
FIGURE 11
Typical cases of interpreted results for Category I and Category II: **(A)** Deformation map and interpreted polygon of a typical case for Category I. **(B)** Field survey results of the typical case for Category I. **(C)** Deformation map and interpreted polygon of a typical case for Category II. **(D)** Field survey results of the typical case for Category II The results of interpreted active landslide and corresponding landslide susceptibility.

data obtained by field investigation, field survey results were then categorized into three groups, as discussed previously. Category I includes 40 interpreted polygons believed to correlate with active landslides. Fourteen interpreted polygons were subsumed into Category II, mainly correlated with anthropogenic activities or soil creep. Category III includes 17 interpreted polygons, which were consistent with Level III.

Field survey results for the baseline and the proposed model are overlayed with interpreted results and illustrated in Figure 9. In Figure 9A, for interpreted results from the baseline model, most of Category I can be recognized correctly. However, several missing recognitions of Category I can be clearly observed, as well as misidentification of Category III. In contrast, as shown in Figure 9B, by applying the proposed model, only two spatial polygons belonging to Category I were not interpreted as active landslide correctly.

Confusion matrices for both the baseline and the proposed model are illustrated in Figure 10. When comparing the performance among different models, the accuracy and recall have similar tendencies. For instance, the accuracy for the proposed model with 5% EP is 0.66, which is better than the baseline model

with an accuracy of 0.61. With the increase of EPs, the accuracy for the proposed model appears slightly degraded. In contrast, the precision of the proposed model is 0.63, which is slightly better than the baseline model with a precision of 0.62. With the increase of EPs, a growing tendency for the precision can be observed. However, from the perspective of practical interests, local authorities and experts would prefer to have false detections (FP) rather than missed ones (FN). From this point of view, the proposed model with 5% EP shows remarkable performance compared to the baseline model. The miss rate (FN divided by the sum of TP and FN) for the proposed model with 5% EP is 0.05, which is only a quarter of the miss rate for the baseline model.

5 Discussion

In order to improve the applicability of InSAR results for rainfall-induced landslide recognition, we assume that rainfall would be a promising indicator to distinguish precursors of slope instability from other ground surface movement phenomena. This hypothesis is based on the causal relationship that in a landslide-prone area

with seasonal precipitation, anomalous ground surface deformation correlated to landslides should primarily be caused by rainfall events necessary to trigger slope instability. Therefore, introducing such a causal relationship in the interpretation process of the InSAR results would be beneficial for model interpretability and applicability for a certain study area.

In order to show and discuss the pros and cons of the proposed method, typical cases of interpreted results for Category I and Category II are depicted in Figure 11. As shown in the Figure 11A, the case of Category I exhibits noticeable ground surface movement in the middle part of the slope. It should be noted that the InSAR results observed a considerable surface deformation, surpassing 50 mm/y, even though the slope direction is nearly perpendicular to the line-of-sight (LOS) direction. By conducting field surveys through the local geomorphic unit (See Figure 11B), distinct deformation was observed in the field as expected. Additionally, from the perspective of slope stability analysis, the surface deformation captured by InSAR implies that the mobility of the active landslide belongs to the thrust type, where the active area is mainly concentrated in the trailing edge. The possible culprit for this case should mainly be attributed to precipitation. However, the influence of irrigation farming in the middle and the human-cutting slope at the toe could not be evaluated without further investigation. Although the above case shows promising recognition of the active landslide using InSAR results, the case of Category II depicts an unexpected misidentification. The slope of the interpreted polygon is in a west-east direction (See Figure 11C), which is consistent with the LOS direction for the ascending orbit. Vegetation coverage in this region is coarse. Therefore, it can be concluded that the observation condition for this case is better than those above. However, field surveys indicated that the possible culprit for this case should be attributed to anthropogenic influences, including irrigation farming and human-cutting slope (See Figure 11D). Even after broadening the survey area and interviewing local citizens, no signs or precursors of landslide triggering can be detected in the field.

Although the performance of the proposed model is inspiring when compared to the baseline model reported in the literature, misclassification cases can still be observed. Possible culprits for misclassification could be attributed to spatial-temporal resolution and accuracy of satellite precipitation products (Brunetti et al., 2018), uncertainties in rainfall thresholds induced by various factors (Segoni et al., 2018), anthropogenic cause contributing to landslide triggering (Xu et al., 2022), and limitations of field investigation to capture subtle signs of ground surface movements (Guzzetti et al., 2012). Therefore, further analysis based on the utilization of cross-validated InSAR results, a combination of satellite precipitation products calibrated with on-site precipitation stations, modification of rainfall thresholds by combining statistical and physical methodology, and improvement of field survey methods are suggested.

6 Conclusion

In this work, a semi-automatic interpretation method for recognizing active landslides induced by rainfall through InSAR results is presented. By constructing empirical rainfall thresholds, the causal relationship between recorded landslide failure events and corresponding rainfall events was introduced into the interpretation

process. The proposed approach is divided into two individual phases, which include unstable regions detection and root-cause analysis. In order to improve the performance of the interpretation method, attempts were made to causally connect rainfall with InSAR-mapped landslide-correlated ground displacement by introducing empirical rainfall thresholds in the latter phase. After validating by field survey, the proposed model utilizing DRI with 5% EP demonstrates a remarkable performance for reducing the miss rate when compared to a baseline model reported in the literature. Although a more extensive validation is necessary, the present interpretation method seems to be very promising from a practical viewpoint for improving large-scale recognition performance for interpreting active rainfall-induced landslide assisted by InSAR results.

Data availability statement

The original contributions presented in the study are included in the article/supplementary material, further inquiries can be directed to the corresponding author.

Author contributions

WL: Conceptualization, Investigation, Methodology, Writing–original draft, Writing–review and editing. PL: Software, Writing–review and editing. YK: Writing–review and editing. LC: Investigation, Writing–review and editing. MaL: Data curation, Investigation, Writing–review and editing. MiL: Data curation, Investigation, Writing–review and editing.

Funding

Acknowledgments

Conflict of interest

The authors declare that the research was conducted in the absence of any commercial or financial relationships that could be construed as a potential conflict of interest.

Publisher's note

All claims expressed in this article are solely those of the authors and do not necessarily represent those of their affiliated organizations, or those of the publisher, the editors and the reviewers. Any product that may be evaluated in this article, or claim that may be made by its manufacturer, is not guaranteed or endorsed by the publisher.

References

Aslan, G., Foumelis, M., Raucoules, D., De Michele, M., Bernardie, S., and Cakir, Z. (2020). Landslide mapping and monitoring using persistent scatterer interferometry (PSI) technique in the French Alps. *Remote Sens.* 12 (8), 1305. doi:10.3390/rs12081305

Bakon, M., Oliveira, I., Perissin, D., Sousa, J. J., and Papco, J. (2017). A data mining approach for multivariate outlier detection in postprocessing of multitemporal InSAR results. *IEEE J. Sel. Top. Appl. Earth Observations Remote Sens.* 10 (6), 2791–2798. doi:10.1109/jstars.2017.2686646

Bekaert, D. P., Handwerger, A. L., Agram, P., and Kirschbaum, D. B. (2020). InSAR-based detection method for mapping and monitoring slow-moving landslides in remote regions with steep and mountainous terrain: an application to Nepal. *Remote Sens. Environ.* 249, 111983. doi:10.1016/j.rse.2020.111983

Brunetti, M. T., Melillo, M., Peruccacci, S., Ciabatta, L., and Brocca, L. (2018). How far are we from the use of satellite rainfall products in landslide forecasting? *Remote Sens. Environ.* 210, 65–75. doi:10.1016/j.rse.2018.03.016

Cai, J., Zhang, L., Dong, J., Guo, J., Wang, Y., Liao, M., et al. (2023). Automatic identification of active landslides over wide areas from time-series InSAR measurements using Faster RCNN *Int. J. Appl. earth observation geoinformation.* 124, 103516. doi:10.1016/j.jag.2023.103516

Chang, L., Dollevoet, R. P., Hanssen, R. F. J. I. j.o.s.t.i.a.e.o., and sensing, r. (2018). Monitoring line-infrastructure with multisensor SAR interferometry: products and performance assessment metrics. *IEEE J. Sel. Top. Appl. Earth Obs. Remote Sens.* 11 (5), 1593–1605. doi:10.1109/jstars.2018.2803074

Cigna, F., Bianchini, S., and Casagli, N. (2013). How to assess landslide activity and intensity with Persistent Scatterer Interferometry (PSI): the PSI-based matrix approach. *Landslides* 10 (3), 267–283. doi:10.1007/s10346-012-0335-7

Crozier, M. J. (1998). The climate landslide couple: a Southern Hemisphere perspective, Paleoclimate. *Research*2, 329–305

Dai, H., Zhang, H., Dai, H., Wang, C., Tang, W., Zou, L., et al. (2022). Landslide identification and gradation method based on statistical analysis and spatial cluster analysis. *Remote Sens.* 14 (18), 4504. doi:10.3390/rs14184504

Di Martire, D., Paci, M., Confuorto, P., Costabile, S., Guastaferro, F., Verta, A., et al. (2017). A nation-wide system for landslide mapping and risk management in Italy: the second Not-ordinary Plan of Environmental Remote Sensing. *Int. J. Appl. earth observation geoinformation* 63, 143–157. doi:10.1016/j.jag.2017.07.018

Dong, J., Niu, R., Li, B., Xu, H., Wang, S. J. G., and Natural Hazards, and Risk (2023). Potential landslides identification based on temporal and spatial filtering of SBAS-InSAR results. *Geomat. Nat. Hazards Risk* 14 (1), 52–75. doi:10.1080/19475705.2022.2154574

Farina, P., Colombo, D., Fumagalli, A., Marks, F., and Moretti, S. (2006). Permanent Scatterers for landslide investigations: outcomes from the ESA-SLAM project. *Eng. Geol.* 88 (3), 200–217. doi:10.1016/j.enggeo.2006.09.007

Ferretti, A., Prati, C., and Rocca, F. (2001). Permanent scatterers in SAR interferometry. *IEEE Trans. geoscience remote Sens.* 39 (1), 8–20. doi:10.1109/36.898661

Festa, D., Bonano, M., Casagli, N., Confuorto, P., De Luca, C., Del Soldato, M., et al. (2022). Nation-wide mapping and classification of ground deformation phenomena through the spatial clustering of P-SBAS InSAR measurements: Italy case study. *ISPRS J. Photogrammetry Remote Sens.* 189, 1–22. doi:10.1016/j.isprsjprs.2022.04.022

Fu, L., Zhang, Q., Wang, T., Li, W., Xu, Q., and Ge, D. (2022). Detecting slow-moving landslides using InSAR phase-gradient stacking and deep-learning network. *Front. Environ. Sci.*, 10. doi:10.3389/fenvs.2022.963322

Gong, W., Hu, M., Zhang, Y., Tang, H., Liu, D., and Song, Q. (2022). GIS-based landslide susceptibility mapping using ensemble methods for Fengjie County in the Three Gorges Reservoir Region, China. *Int. J. Environ. Sci. Technol.* 19 (8), 7803–7820. doi:10.1007/s13762-021-03572-z

Guzzetti, F., Mondini, A. C., Cardinali, M., Fiorucci, F., Santangelo, M., and Chang, K.-T. (2012). Landslide inventory maps: new tools for an old problem. *Earth-Science Rev.* 112 (1), 42–66. doi:10.1016/j.earscirev.2012.02.001

Guzzetti, F., Peruccacci, S., Rossi, M., and Stark, C. P. (2007). Rainfall thresholds for the initiation of landslides in central and southern Europe. *Meteor. Atmos. Phys.*, 98 (3), 239–267. doi:10.1007/s00703-007-0262-7

He, Y., Wang, W., Zhang, L., Chen, Y., Chen, Y., Chen, B., et al. (2023). An identification method of potential landslide zones using InSAR data and landslide susceptibility. *Geomatics, Nat. Hazards Risk* 14 (1). doi:10.1080/19475705.2023.2185120

Ho Tong Minh, D., Hanssen, R., and Rocca, F. J. R. S. (2020). Radar interferometry: 20 years of development in time series techniques and future perspectives. *Remote Sens. (Basel).* 12 (9), 1364. doi:10.3390/rs12091364

Intrieri, E., Carlà, T., and Gigli, G. (2019). Forecasting the time of failure of landslides at slope-scale: A literature review. *Earth-Science Rev.*, 193, 333–349. doi:10.1016/j.earscirev.2019.03.019

Jia, H., Wang, Y., Ge, D., Deng, Y., and Wang, R. (2022). InSAR study of landslides: early detection, three-dimensional, and long-term surface displacement estimation—a case of Xiaojiang River Basin, China. *Remote Sens.* 14 (7), 1759. doi:10.3390/rs14071759

Lacroix, P., Handwerger, A. L., and Bièvre, G. (2020). Life and death of slow-moving landslides. *Nat. Rev. Earth and Environ.* 1 (8), 404–419. doi:10.1038/s43017-020-0072-8

Leonarduzzi, E., Molnar, P., and McArdell, B. W. J. W. R. R. (2017). Predictive performance of rainfall thresholds for shallow landslides in S witzerland from gridded daily data. *Water Resour. Res.* 53 (8), 6612–6625. doi:10.1002/2017wr021044

Li, B., Gao, Y., Yin, Y., Wan, J., He, K., Wu, W., et al. (2022). Rainstorm-induced large-scale landslides in northeastern chongqing, China, august 31 to september 2, 2014. *Bull. Eng. Geol. Environ.* 81 (7), 271. doi:10.1007/s10064-022-02763-3

Li, J., Xing, X., Ou, J. J. B. o.E. G., and Environment, t. (2023). Locating and characterizing potential rainfall-induced landslides on a regional scale based on SBAS-InSAR technique. *Bull. Eng. Geol. Environ.* 82 (8), 329. doi:10.1007/s10064-023-03356-4

Liang, J., Dong, J., Zhang, S., Zhao, C., Liu, B., Yang, L., et al. (2022). Discussion on InSAR identification effectivity of potential landslides and factors that influence the effectivity. *Remote Sens.* 14 (8), 1952. doi:10.3390/rs14081952

Liu, R., Ding, Y., Sun, D., Wen, H., Gu, Q., Shi, S., et al. (2023). Insights into spatial differential characteristics of landslide susceptibility from sub-region to whole-region cased by northeast Chongqing, China. *Geomatics, Nat. Hazards Risk.* 14 (1), 2190858. doi:10.1080/19475705.2023.2190858

Loche, M., Alvioli, M., Marchesini, I., Bakka, H., and Lombardo, L. (2022). Landslide susceptibility maps of Italy: lesson learnt from dealing with multiple landslide types and the uneven spatial distribution of the national inventory. *Earth-Science Rev.* 232, 104125. doi:10.1016/j.earscirev.2022.104125

Lu, P., Bai, S., Tofani, V., and Casagli, N. (2019). Landslides detection through optimized hot spot analysis on persistent scatterers and distributed scatterers. *ISPRS J. Photogrammetry Remote Sens.* 156, 147–159. doi:10.1016/j.isprsjprs.2019.08.004

Melillo, M., Brunetti, M. T., Peruccacci, S., Gariano, S. L., and Guzzetti, F. (2015) An algorithm for the objective reconstruction of rainfall events responsible for landslides*landslides*, 12 (2), 311–320. doi:10.1007/s10346-014-0471-3

Melillo, M., Brunetti, M. T., Peruccacci, S., Gariano, S. L., Roccati, A., and Guzzetti, F. (2018). A tool for the automatic calculation of rainfall thresholds for landslide occurrence. *Environ. Model. and Softw.* 105, 230–243. doi:10.1016/j.envsoft.2018.03.024

Milillo, P., Sacco, G., Di Martire, D., and Hua, H. (2022). Neural network pattern recognition experiments toward a fully automatic detection of anomalies in InSAR time series of surface deformation. *Front. Earth Sci.* 9, 728643. doi:10.3389/feart.2021.728643

Montalti, R., Solari, L., Bianchini, S., Del Soldato, M., Raspini, F., and Casagli, N. (2019). A Sentinel-1-based clustering analysis for geo-hazards mitigation at regional scale: a case study in Central Italy. *Geomatics, Nat. Hazards Risk* 10 (1), 2257–2275. doi:10.1080/19475705.2019.1690058

Necula, N., Niculiță, M., Fiaschi, S., Genevois, R., Riccardi, P., and Floris, M. (2021). Assessing urban landslide dynamics through multi-temporal InSAR techniques and slope numerical modeling. *Remote Sens.* 13 (19), 3862. doi:10.3390/rs13193862

Nguyen, P., Shearer, E. J., Tran, H., Ombadi, M., Hayatbini, N., Palacios, T., et al. (2019). The CHRS Data Portal, an easily accessible public repository for PERSIANN global satellite precipitation data. *Sci. Data* 6, 180296. doi:10.1038/sdata.2018.296

Nie, Y., and Sun, J. (2020). Evaluation of high-resolution precipitation products over southwest China. *J. Hydrometeorol.* 21 (11), 2691–2712. doi:10.1175/jhm-d-20-0045.1

Notti, D., Herrera, G., Bianchini, S., Meisina, C., García-Davalillo, J. C., and Zucca, F. (2014). A methodology for improving landslide PSI data analysis. *Int. J. Remote Sens.* 35 (6), 2186–2214. doi:10.1080/01431161.2014.889864

Novellino, A., Cesarano, M., Cappelletti, P., Di Martire, D., Di Napoli, M., Ramondini, M., et al. (2021). Slow-moving landslide risk assessment combining Machine Learning and InSAR techniques. *CATENA.*105317. doi:10.1016/j.catena.2021.105317

Pedregosa, F., Varoquaux, G., Gramfort, A., Michel, V., Thirion, B., Grisel, O., et al. (2011). Scikit-learn: machine learning in Python. *J. Mach. Learn. Res.* 12, 2825–2830. doi:10.5555/1953048.2078195

Ponziani, F., Ciuffi, P., Bayer, B., Berni, N., Franceschini, S., and Simoni, A. (2023). Regional-scale InSAR investigation and landslide early warning thresholds in Umbria, Italy. *Eng. Geol.* 327, 107352. doi:10.1016/j.enggeo.2023.107352

Pu, C., Xu, Q., Wang, X., Li, Z., Chen, W., Zhao, K., et al. (2023). Refined mapping and kinematic trend assessment of potential landslides associated with large-scale land creation projects with multitemporal InSAR. *Int. J. Appl. Earth Observation Geoinformation* 118, 103266. doi:10.1016/j.jag.2023.103266

Raspini, F., Bianchini, S., Ciampalini, A., Del Soldato, M., Solari, L., Novali, F., et al. (2018). Continuous, semi-automatic monitoring of ground deformation using Sentinel-1 satellites. *Sci. Rep.* 8 (1), 7253. doi:10.1038/s41598-018-25369-w

Righini, G., Pancioli ∗ ∗ , V., and Casagli, N. (2012). Updating landslide inventory maps using Persistent Scatterer Interferometry (PSI). *Int. J. Remote Sens.* 33 (7), 2068–2096. doi:10.1080/01431161.2011.605087

Rossi, M., Luciani, S., Valigi, D., Kirschbaum, D., Brunetti, M. T., Peruccacci, S., et al. (2017). Statistical approaches for the definition of landslide rainfall thresholds and their uncertainty using rain gauge and satellite data. *Geomorphology* 285, 16–27. doi:10.1016/j.geomorph.2017.02.001

Segoni, S., Piciullo, L., and Gariano, S. L. (2018). A review of the recent literature on rainfall thresholds for landslide occurrence. *Landslides* 15 (8), 1483–1501. doi:10.1007/s10346-018-0966-4

van Natijne, A. L., Bogaard, T., van Leijen, F. J., Hanssen, R. F., and Lindenbergh, R. C. (2022). World-wide InSAR sensitivity index for landslide deformation tracking. *Int. J. Appl. earth observation geoinformation*, 111.102829. doi:10.1016/j.jag.2022.102829

Varnes, D. J. (1984). Landslide hazard zonation: a review of principles and practice. Paris: UNESCO

Wang, Y., Liu, D., Dong, J., Zhang, L., Guo, J., Liao, M., et al. (2021). On the applicability of satellite SAR interferometry to landslide hazards detection in hilly areas: a case study of Shuicheng, Guizhou in Southwest China. *Landslides* 18, 2609–2619. doi:10.1007/s10346-021-01648-y

Wasowski, J., and Bovenga, F. (2014). Investigating landslides and unstable slopes with satellite Multi Temporal Interferometry: current issues and future perspectives. *Eng. Geol.* 174, 103–138. doi:10.1016/j.enggeo.2014.03.003

Xiong, Z., Zhang, M., Ma, J., Xing, G., Feng, G., and An, Q. J. L. (2023). InSAR-based landslide detection method with the assistance of C-index. *Landslides* 20 (12), 2709–2723. doi:10.1007/s10346-023-02120-9

Xu, Q., Zhao, B., Dai, K., Dong, X., Li, W., Zhu, X., et al. (2023). Remote sensing for landslide investigations: a progress report from China. *Eng. Geol.* 321, 107156. doi:10.1016/j.enggeo.2023.107156

Xu, Y., Lu, Z., and Leshchinsky, B. J. J. o.G. R. E. S. (2022). Kinematics of irrigation-induced landslides in a Washington Desert: impacts of basal geometry. *JGR. Earth Surf.* 127 (2), e2021JF006355. doi:10.1029/2021jf006355

Zhang, W., He, Y., Wang, L., Liu, S., and Meng, X. (2023). Landslide Susceptibility mapping using random forest and extreme gradient boosting: a case study of Fengjie, Chongqing. *Geol. J.* 58 (6), 2372–2387. doi:10.1002/gj.4683

Zhang, Y., Meng, X., Chen, G., Qiao, L., Zeng, R., and Chang, J. (2016). Detection of geohazards in the Bailong River Basin using synthetic aperture radar interferometry. *Landslides* 13, 1273–1284. doi:10.1007/s10346-015-0660-8

Zhang, Y., Meng, X., Jordan, C., Novellino, A., Dijkstra, T., and Chen, G. (2018). Investigating slow-moving landslides in the Zhouqu region of China using InSAR time series. *Landslides* 15, 1299–1315. doi:10.1007/s10346-018-0954-8